Journal of Marine Science and Technology

Volume 21 | Issue 4 Article 12

COMPARISON OF DIFFERENT WIND STRESS EFFECTS ON SST AND SSS IN THE EAST CHINA SEA REGION

Hung-Jen Lee
Department of Marine Environmental Informatics, National Taiwan Ocean University, Keelung, Taiwan, R.O.C, lecgyver@mail.ntou.edu.tw

Shih-Jen Huang
Department of Marine Environmental Informatics, National Taiwan Ocean University, Keelung, Taiwan, R.O.C

Shenn-Yu Chao
Horn Point Laboratory, University of Maryland Center for Environmental Science, Cambridge, MD, USA

Kon-Kee Liu
Institute of Hydrological and Oceanic Sciences, National Central University, Jungli, Taiwan, R.O.C.

COMPARISON OF DIFFERENT WIND STRESS EFFECTS ON SST AND SSS IN THE EAST CHINA SEA REGION

Acknowledgements

Author H.J.L. was sponsored by the National Science Council (Taiwan) through grants NSC-100-2611-M-019-003.

Journal of Marine Science and Technology, Vol. 21, No. 4, pp. 469-482 (2013)
DOI: 10.6119/JMST-013-0508-1

COMPARISON OF DIFFERENT WIND STRESS EFFECTS ON SST AND SSS IN THE EAST CHINA SEA REGION

Hung-Jen Lee[1], Shih-Jen Huang[1], Shenn-Yu Chao[2], and Kon-Kee Liu[3]

Key words: wind stress, equivalent depth of fresh water, amphidromic systems.

ABSTRACT

Ocean circulations closely associated with the changes of wind system are investigated using a three-dimensional tide-circulated coupling model. Based on the coupling model, we apply different wind datasets, to some extent reflecting wind system variations associated with global climate change, but constant monthly temperature and salinity fields to assess the effect of differing wind strength stresses in the East China Sea region, leading to significant influences on hydrographic fields. In the model based on the Hellman-Rosenstein wind dataset, more distant from the mouth of the Changjiang River (Yangtze River), the Yellow Sea Warm Current strengthens because of the wind stress; weaker wind stresses may reduce the strength of the Yellow Sea Warm Current, resulting in it retreating along its path. The modeled results suggest that there is at least a 1.5°C anomaly in temperature and a 2 psu anomaly in salinity between the Changjiang River mouth and the Korean Peninsula when different wind fields are imposed in the model. The major differences in the sea surface temperature (SST) and the sea surface salinity (SSS) fields usually occur between latitudes 30°N and 35°N, which coincides with the regions having the steepest north-south temperature gradient.

I. INTRODUCTION

The East China Sea (ECS), the Yellow Sea (YS) and the Bohai Sea (BS) are interconnected off the east coast of China (the so-called ECS region) to form a series of shallow marginal seas extending from 25°N to 41°N (Fig. 1). Among the ECS, YS and BS, the ECS is the largest and is the only sea open to the western Pacific Ocean to the east; the Sea of Japan is to the northeast of the ECS and the Taiwan Strait is to the southwest. In the ECS region, many studies have confirmed the major current circulation characteristics through observations and ocean models [3, 4, 11, 15, 16, 19]. These studies have shown that the main stream of the Kuroshio Current (KC) flows northeastward following the 200 m curved isobaths along the continental slope of the ECS. In addition, the Taiwan Warm Current (TWC) flows through the Taiwan Strait and enters the ECS [1]. According to historical data, neither the YS nor the BS has major currents driving circulation in summer, which appears to be related to a weak current (the YS Warm Current; YSWC) that flows northwestward from Jeju Island to

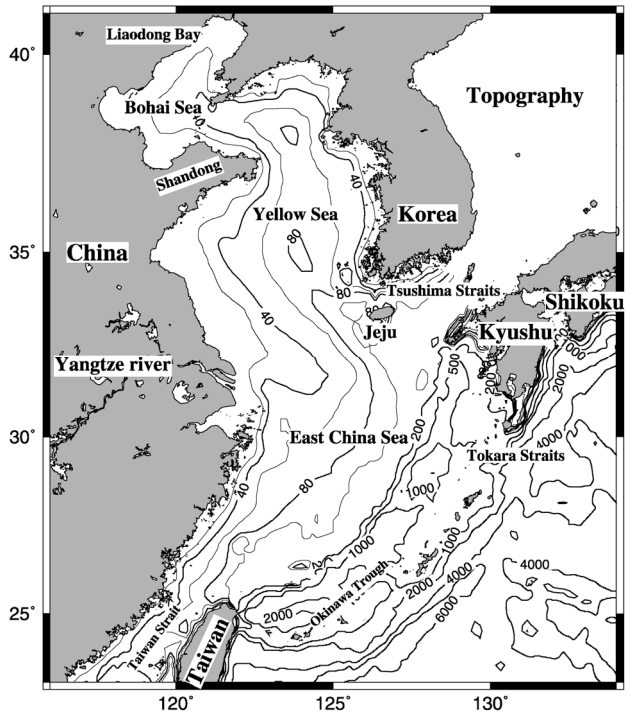

Fig. 1. Model domain and topography (in meters) of the East China Sea and adjacent seas excluding the Sea of Japan.

Paper submitted 11/25/12; revised 05/01/13; accepted 05/08/13. Author for correspondence: Hung-Jen Lee (e-mail: lecgyver@mail.ntou.edu.tw).
[1] *Department of Marine Environmental Informatics, National Taiwan Ocean University, Keelung, Taiwan, R.O.C.*
[2] *Horn Point Laboratory, University of Maryland Center for Environmental Science, Cambridge, MD, USA.*
[3] *Institute of Hydrological and Oceanic Sciences, National Central University, Jungli, Taiwan, R.O.C.*

Shandong Peninsula in winter [11]. Tides in the world oceans dissipate a large amount of tidal energy (more than 3 terawatts), including approximately 1 terawatt dissipated through conversion to baroclinic motion, particularly in shallow marginal seas including the ECS and adjacent seas. The tidal amplitude over deep water is usually small, but increases abruptly as tidal waves propagate near shallow water areas, as occur in the ECS and adjacent seas. This strong tidal energy could lead to mixing between the surface layer and the main thermocline, and also influence the circulation in seas of the ECS region. Tidal effects on circulation are potentially important in this region, particularly in relation to interactions with the Changjiang River (Yangtze River) plumes. Therefore, in this study we incorporated tidal currents into a previously validated three-dimensional (3-D) subtidal circulation model [12], to generate a tide-circulated coupling model. However, the circulation of surface or subsurface water in the three seas of the ECS system is mainly driven by the East Asia monsoon. The prevailing winds are predominantly southeasterly from July to mid-September, at which time the wind direction changes to easterly and then to northeasterly; these conditions prevail until April of the following year [17]. Although the prevailing winds in winter are northeasterly below latitude 30°N, northwesterly winds occur in the northern part of the study area [11]. Hence, winds in this region are particularly important, especially in coupled estuary-shelf environments. Winds, tides and river discharges are the three primary forcings that drive estuarine circulation [2]. Historical observations have shown that freshwater entering the estuary forms a thin plume that floats over the denser seawater. The physical layering of the freshwater and the saline seawater enables the plume to be easily moved by local winds. For instance, Choi and Wilkin [5] studied wind effects on the dispersal of Hudson River plumes, using a 3-D and regional ocean modeling system. Their results show that a northward wind favorable to upwelling causes offshore displacement of a previously formed coastally trapped plume, and drives the plume along the Long Island coast. When the wind blows southward, favoring downwelling, the wind induces a narrow coastal jet that drives the diluted water plume further south along the New Jersey coast. Similarly, when northeasterly winds prevail in winter the Changjiang diluted water (CDW) forms a narrow band of low salinity water that follows the China Coastal Current (CCC) to the south, in some cases to north of the Taiwan Strait [11, 12]. A number of global wind stress datasets are commonly used as the sea-surface driving force in general circulation models. Amongst these are the more than 100-year monthly average dataset of Hellerman and Rosenstein (HR) [9], the 27-year monthly average dataset of the National Centers for Environmental Prediction (NCEP Reanalysis dataset retrieved from http://www.cdc.noaa.gov/cdc/data.ncep.reanalysis2.html#sktnote), and the daily QSCAT wind data. In the present study, we compare the HR and NCEP wind datasets of global wind stress as forcing factors in our ocean model. The HR dataset contains monthly averaged observations for the years 1870-1976. The data are based on a 2° latitude × 2° longitude grid, and are derived from > 35 million surface observations covering the world ocean. The NCEP wind dataset is averaged from 1979 to 2006; the NCEP produces regular weather forecasts and uses reanalysis of older data to generate consistent meteorological information. The two wind stress datasets serve as the fields for establishing sea surface boundary conditions for the model. We use the tide-circulated coupling model to assess how different wind stresses affect the sea surface temperature (SST), the sea surface salinity (SSS) and the equivalent depth of freshwater in the ECS region. We also assess how the single model used in the study responds to forcing under the different wind stress datasets. This comparison enables assessment of the similarities and differences when the HR and NCEP wind datasets are used in the model, and whether the ocean response could be predicted using these wind stress data as a driving force at the sea surface.

II. TIDE-CIRCULATED COUPLING MODEL

To account for the scale of motion being considered, a tide-circulated coupling model is used to solve 3-D temperature, salinity and momentum equations under hydrostatic and Boussinesq approximations. The ocean motion is governed by the equations written as follows:

$$\frac{Du}{Dt} - fv = -\frac{1}{\rho_o} p_x + A_M \nabla^2 u + \kappa u_{zz} + \tau_{sx} - \tau_{bx} \tag{1}$$

$$\frac{Dv}{Dt} + fu = -\frac{1}{\rho_o} p_y + A_M \nabla^2 v + \kappa v_{zz} + \tau_{sy} - \tau_{by} \tag{2}$$

$$p_z = -\rho g \tag{3}$$

where u and v are the velocities in the x and y directions, respectively, g is a constant, known as gravitational acceleration, ρ is the density, ρ_o is a reference water density, τ_{sx} and τ_{sy} are the wind stresses at the sea surface in the x and y directions, respectively, τ_{bx} and τ_{by} are the bottom frictions in the x and y directions, respectively, and A_M and κ are the horizontal and vertical mixing coefficients for the momentum equations, respectively. D/Dt in Eqs. (1) and (2) is a nonlinear term operator, and P_x, P_y and P_z are the partial derivatives of the pressure term with respect to x, y and z in the horizontal and vertical directions, respectively.

The conservation equations for temperature (T) and salinity (S) are:

$$\partial_t T + v\nabla T + w\partial_z T = \theta + r(T^* - T), \tag{4}$$

$$\partial_t S + v\nabla S + w\partial_z S = \delta + r(S^* - S), \tag{5}$$

where θ and δ are mixing terms, v is the horizontal velocity

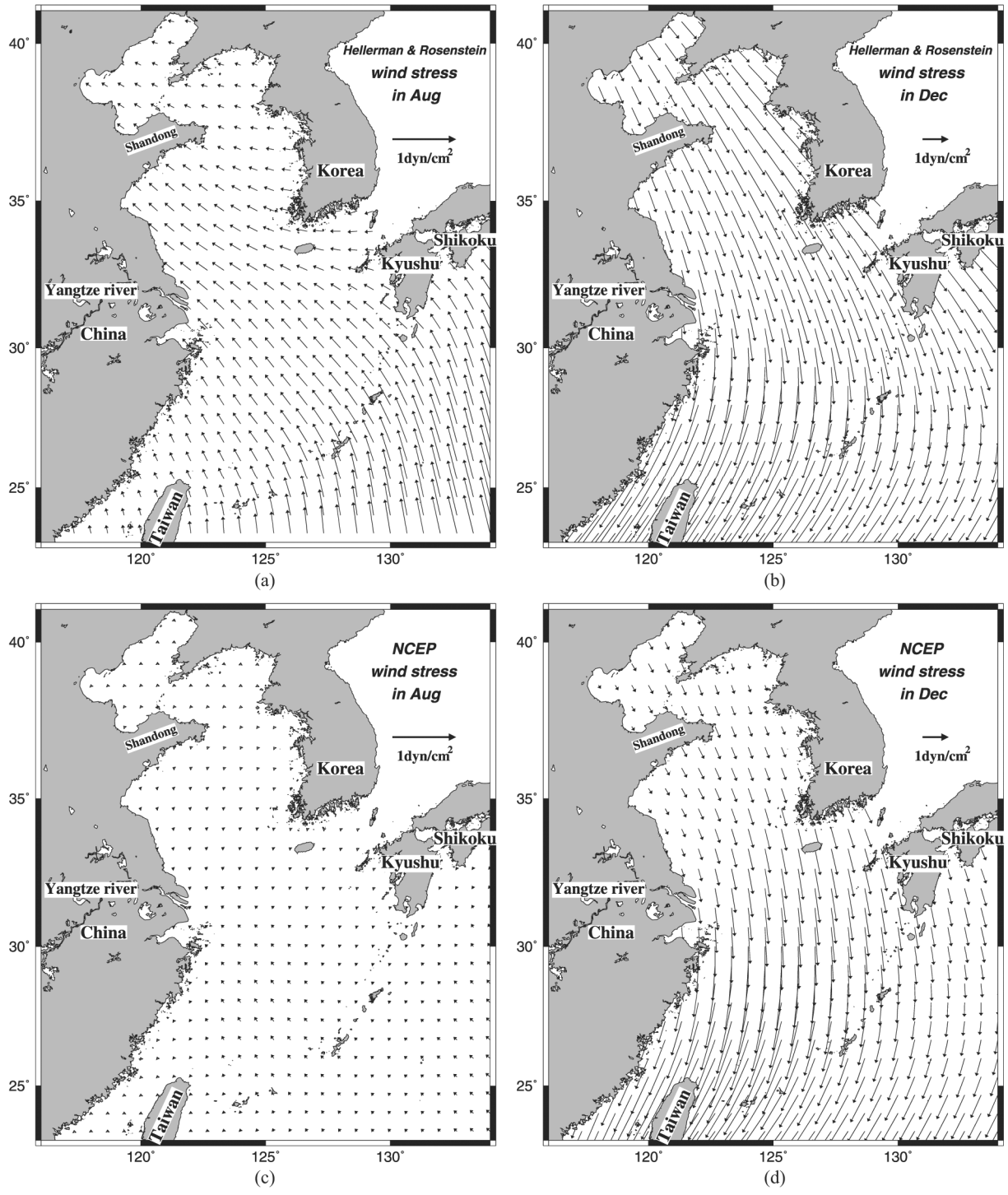

Fig. 2. Monthly climatological wind stress fields derived from the HR dataset for (a) summer and (b) winter, and from the NCEP dataset in (c) summer and (d) winter.

vector, and w is the vertical velocity. Following Sarmiento and Bryan [21], we progressively nudge the values for temperature and salinity in Eqs. (4) and (5), respectively, slowly toward their respective climatologic values T^* and S^* (the global WOA climatology, 2005), with a latitude-dependent restoration rate (r). Their magnitude between 0 and 30 m is approximately 1/50 day^{-1} at 32°N latitude, and increases to the north and south from 1/50^{-1} (32°N) to 1/10 day^{-1} at 23°N and 41°N, respectively. Moreover, the restoration rate is 0 between 30 and 150 m, and 1/15 day^{-1} below 150 m. In the thermocline, this measure enables it to move freely. In addition, the nudging calculation becomes diagnostic if r is

Table 1. Monthly transports (Sv) through open ocean boundaries. Positive and negative values are for inflow and outflow, respectively.

Month	Jan	Feb	Mar	Apr	May	Jun	Jul	Aug	Sep	Oct	Nov	Dec
Taiwan Strait	0.5	0.5	1.5	1.5	2.2	2.3	2.3	2.4	2.4	1.5	0.5	0.5
Kuroshio Inflow	22.0	22.0	22.5	23.0	24.0	23.5	23.5	28.0	28.0	22.0	21.0	22.0
Kuroshio Outflow	-20.24	-20.62	-22.27	-22.63	-23.96	-23.04	-22.53	-26.74	-26.59	-19.83	-18.2	-19.72
Tsushima Straits	-2.27	-1.89	-1.75	-1.89	-2.28	-2.80	-3.32	-3.71	-3.85	-3.71	-3.33	-2.80

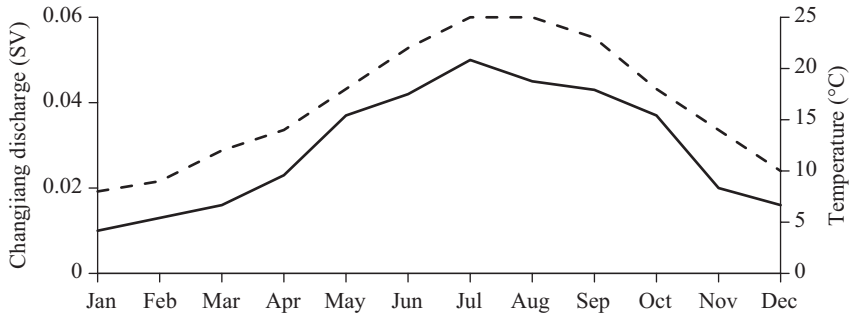

Fig. 3. Monthly mean inflow (solid line) and temperature (dashed line) of the Changjiang River, as compiled by the Global Runoff Data Center of the Federal Institute of Hydrology, Germany.

excessively large and prognostic if r is small. The procedure for these calculations is described in more detail in Lee and Liu [13].

The study area is extended from latitude 23°N to 41°N and from longitude 118°E to 134°E with a horizontal resolution of 1/6°; $\Delta x = \Delta y =$ approximately 18.5 km; and the total grid includes 109 × 109 points in the horizontal direction. In the tide-circulated coupling model, Δt is 8 s for the barotropic mode, and ΔT is 400 s for the baroclinic mode. Because both times are much smaller than the M_2 tidal period (12.42 h), the model only requires calculation of the baroclinic set of equations once every 50 barotropic calculations. Apart from sea level variations, the top layer is set to 5 m thick, but is subject to adjustment for sea level variations. Beneath the surface layer the thickness of each layer is 85% of the thickness of the layer immediately below. The maximum depth is 6018 m and there are 33 layers in the vertical direction. The horizontal mixing coefficient is 5000 $m^2\ s^{-1}$ for momentum, and 50 $m^2\ s^{-1}$ for temperature and salinity equations. The quadratic bottom friction coefficient is 0.0015 which is a more appropriate value considering the semidiurnal tide [8]. Therefore, the value of the sea bed drag coefficient is adopted and fixed through all model runs during the study.

The monthly climatological wind stresses from the HR and NCEP datasets are applied serving as a driving force at the sea surface in the ocean model. In Fig. 2 the top two panels show the HR wind stress data (Figs. 2(a) and 2(b)), and the bottom two panels show the NCEP wind stress data (Figs. 2(c) and 2(d)), for summer and winter, respectively. In summer, the HR wind stress is much stronger than that for the NCEP, but for each the strong northwesterly/northeasterly monsoon is almost the same strength during winter, although the NCEP wind stress is somewhat weaker in the regions of the YS and BS. Table 1 shows the mean monthly inflows and outflows through the open ocean boundaries (for justifications, see Lee and Chao [11]). Fig. 3 shows the monthly mean inflow, temperature and salinity for the Changjiang River discharge, as compiled by the Global Runoff Data Center of the Federal Institute of Hydrology, Germany [12].

In addition, we simultaneously impose tidal heights and currents on the open boundaries using the results from a two-dimensional barotropic tidal model having a 1/12° resolution [10] and a tide-induced sea level with 6 tidal constituents (P_1, O_1, K_1, N_2, M_2 and S_2), according to the equation:

$$\varsigma = \sum_{n=1}^{6} f_n \varsigma_n \cos(\omega_n t + \theta_n), \tag{6}$$

where f_n is the nodal factor (assumed to be unity), ω_n is the frequency of the tidal constituents, and θ_n is the phase lag of the tidal constituents. Unlike other studies including those of Guo and Yanagi [8] and Yanagi *et al*. [23], the focus of the present study is time-independent sea level variations. However, we did not intend to simulate a real ocean, or to directly compare the model results with observations.

Assuming linearity [6, 20], corresponding tidal currents are related to the instantaneous sea level as below.

$$V_t = (g/D)^{\frac{1}{2}} \sum_{n=1}^{6} f_n \varsigma_n \cos(\omega_n t + \theta_n), \tag{7}$$

where D is the undisturbed water depth at the open boundaries, and g is the gravitational acceleration.

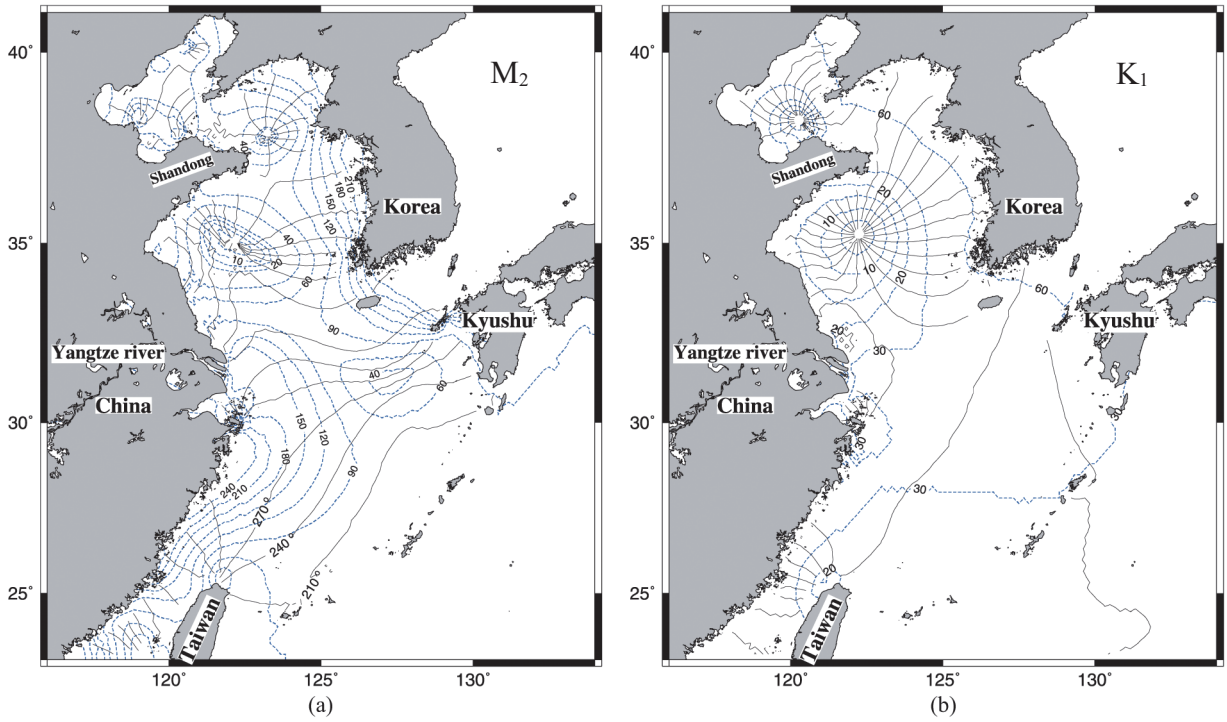

Fig. 4. Model-calculated co-tidal (solid line) and co-range (dashed line) charts of (a) M_2 and (b) K_1 tides.

Hence, the water flow penetrating each open inflow/outflow boundary in the 3-D model is concurrently driven by the monthly mean currents (V_m) and the tidal currents (V_t) according to:

$$V_n = V_m + V_t$$

where V_n is the normally flow transport through the open boundary with no gradient.

Commencing from a state of rest water, we ran the two models, i.e., the HR wind-driven model and the NCEP wind-driven model, with tides for two years to avoid the effects of initial transients, and used the two-year result to facilitate the following discussion.

III. MODEL CO-TIDAL AND CO-RANGE CHARTS

Based on the suggestions of Guo and Yanagi [8] and Lefevre *et al*. [14], we adopt the bed drag coefficient C_d = 0.0015 for all model runs in this study. The modeled sea level fields are harmonically decomposed for each major tidal constituent using the program of Foreman [7], and are obtained from the corresponding major tidal co-phase and co-range constituents in the ECS region. The co-phase and co-range charts are drawn by way of harmonic analysis using the results of the coupling model. Fig. 4 partially shows the calculated co-phase and co-range charts. Our coupling model successfully reproduces two amphidropic points, in the BS and its northern reach (Liaodong Bay), and two amphidromic points in the YS for M_2 tides (Fig. 4(a)); these results approximate those of Guo and Yanagi [8] and Lefevre *et al*. [14], and particularly the model results of Lefevre *et al*. [14]. The results of Lefevre *et al*. [14] for major semidiurnal tides show that along the coast of China to the south of the Changjiang mouth (CM), a number of co-phase lines extend from south of the CM to latitude 34°N on the China coast (figure not shown). These do not link to the center of the amphidromic point, which is a similar result to that of our model for M_2 and S_2. In addition, one amphidromic point appears in the southern BS and another in Liaodong Bay, which is inferior to the point in the northern BS because of an incomplete amphidromic system, as shown in Fig. 4(a). The modeled M_2 amplitude off the west Korean peninsula and in front of the CM is large, and resembles the model results of Wu *et al*. [22] and Guo and Yanagi [8]. Our model also effectively reproduces two amphidromic points for K_1 tides, one of which is evident in the YS to the south of Shandong peninsula, and the other is evident to the north of the peninsula (Fig. 4(b)). The development of major diurnal tides is superior to that of the major semidiurnal tides in co-phase amphidromic systems. In addition to comparison with the tidal model results in other reports, our calculated results are consistent with observational data, including the amphidromic points and the magnitude of the co-range in relation to the location.

The two amphidromic points have been reproduced by a number of tidal models as a measure of accuracy [8]; however, in some modeling experiments the points have not been

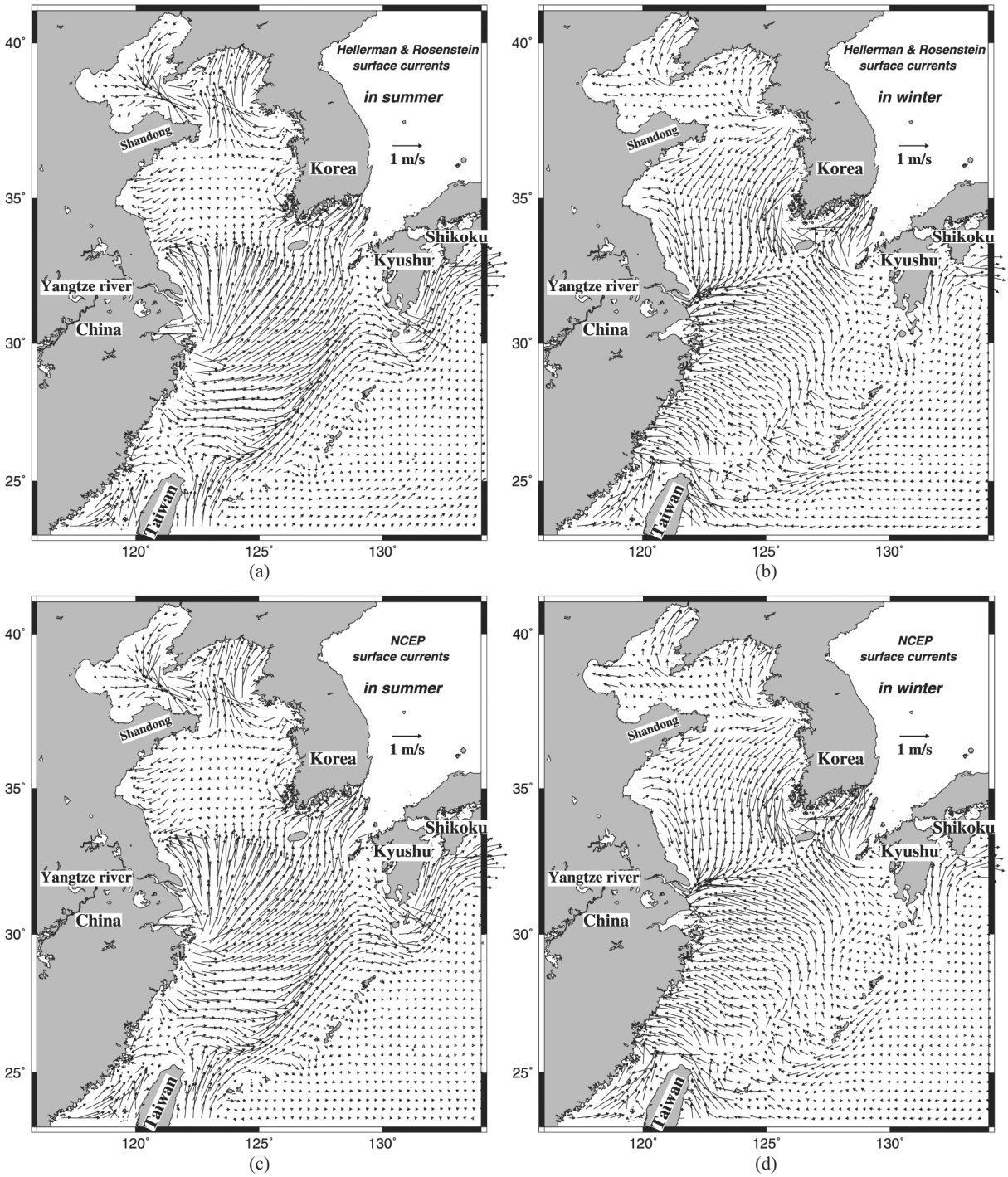

Fig. 5. Model-derived surface flow fields for the HR wind-driven model in (a) summer and (b) winter, and for the NCEP wind-driven model in (c) summer and (d) winter.

reproduced at the same locations. Therefore, the presence of the M_2 amphidromic points in the BS and Liaodong Bay has been used as a criterion by many investigators to indicate whether a model has produces a successful simulation. Apparently, the target must be met using a set of parameters that are costly to measure, among which the most important are bed drag coefficient, grid size, and accurate representations of the coastline and bottom bathymetry. Our modeling results indicate that diurnal amphidromic systems are to better develop than semidiurnal ones. This is understandable, because, through discretization, numerical models resolve longer waves better. South of Shandong peninsula the active tidal wave propagates as coastal Kelvin waves whether it leads to the conspicuous absence of amphidromic points.

Under the same conditions (including the same initial hydrographic data and tidal constituents, but different winds) we compare the effects of each wind field acting at the sea surface. Various hydrographic features of the model results are presented below.

IV. CIRCULATION FEATURES IN DIFFERENT SEASONS

Unlike the flow fields in the general circulation model, those in the tide-circulated coupling model change direction haphazardly in the open ocean, but reverse their direction approximately every 6 hours near the coastal zone. Here we present the flow fields using only instantaneous data of the model output. Fig. 5 shows an instantaneous snapshot of model-derived circulation at 2.5 m depth for the HR wind-driven model (top panels) and the NCEP wind-driven model (bottom panels) in summer and winter, respectively. Fig. 5 shows that the tide-circulating flow fields in summer (left panels) and winter (right panels) met our expectations. Off northeast Taiwan, part of the KC intrudes onto the continental shelf of the ECS, forming a large loop, and then returns to its main stream. The major part of the current turns from the north to the northeast, and thereafter continues to follow the shelf break. In winter, the KC apparently disappears in the surface currents, but merges into the subsurface layer and flows northeastward as usual [12]. In addition, the wind-driven surface current flows southwest along right hand side of the Okinawa Islands. In light of the past extensive literatures, the TWC enters the ECS from the Taiwan Strait, and turns eastward to join the main stream of the KC at approximately 28°N. The TWC apparently becomes stronger in the southern Taiwan Strait and weaker (or disappears) in the northern Taiwan Strait. Strongly tidal currents replace the moderate TWC in the Taiwan Strait. Between the BS and the north of the YS the strong tidal currents move forward and backward, especially in the neck of the Straits. And, strong tidal currents that flow south along the shore are also evident adjacent to the coast of China and to the west of the Korean peninsula. A major divergent/convergent center occurs around the CM.

In general, the model-derived surface currents in the ECS region are strong as a result of the large amplitude of sea level elevation, especially in the shallower waters along the coast. Lefevre *et al*. [14] summarized that the tidal elevations could reach 3 m in Hanchow Bay, 3.7 m in BS, 8.5 m in Incheon Bay, and approximately 5.6 m on the mid west coast of Taiwan. The corresponding tidal currents are likely to be very strong. Therefore, the flows are usually very strong in the shelf areas of the ECS region, but beyond the Okinawa Islands in the western Pacific Ocean the flow speed is much weaker.

The differences in the model-derived surface currents between the HR (Figs. 5(a) and 5(b)) and the NCEP (Figs. 5(c) and 5(d)) models are minor except to the east of the Okinawa Islands where the current reflects that the HR wind-driven reverse flows are somewhat stronger than those for the NCEP in winter. In summer, although the NCEP winds are weaker than the HR winds, the differences between the model-derived surface currents are small. It is revealed that the tidal forcing is found to dominate the currents in the ECS region; for example, the CCC becomes inconspicuous in winter, which should be disturbed and constrained by the strongly tidal forces.

V. SURFACE TEMPERATURE FIELDS

Fig. 6 shows instantaneous snapshots of the model-derived surface circulation superimposed on the model-derived surface temperature for the HR wind-driven model (top panels) and the NCEP wind-driven model (bottom panels) in summer and winter, respectively. Each model-derived surface temperature (Figs. 6(a) and 6(c)) show two relatively low temperature regions, implying the presence of upwelling activity off the southwestern Korean peninsula and to the north of the CM in summer. The lowest temperature in the center of the upwelling regions is approximately 19°C. Meanwhile, the temperature of the CDW in summer manifests a little warmer than its vicinity. Figs. 6(a) and 6(c) also indicate that a temperature front is deflected from south of the CM to the Tsushima Straits. Another noteworthy feature (Figs. 6(a) and 6(c)) is a narrow band of coastal upwelling along the southeastern coast of China, extending from south of the CM to north of the Taiwan Strait. The temperature in this band is significantly lower than in waters to the east. In addition, wind-derived upwelling in the NCEP model seems stronger than that in the HR model, and then the lowest temperature (26°C in Fig. 6(c)) is in the narrow band extending from south of the CM to northwest of the Taiwan Strait, but the 26°C isotherm fails to see in Fig. 6(a). This implies that southwesterly winds may reduce the strength of coastal upwelling along the southeastern coast of China. It is noteworthy that the northeast flow of the KC in summer closely matches the temperature fields in Figs. 6(a) and 6(c). Fig. 7 is derived from monthly climatological SST data from the terra MODIS (Moderate Resolution Imaging Spectroradiometer) satellite, which has a ground resolution of 4 km. The SST data for the plots in Fig. 7 are averaged over at least 12 years (from 2000 to 2011, or from 2000 to 2012). Fig. 7(a) shows that the temperature to the north of the YS and the BS is colder than approximately 24°C, and is generally relatively warm south of latitude 35°N, especially in the path of the KC, where the temperature is in the order of 30°C. The monthly climatological SST from the satellite data for the northern YS and the BS in summer is approximately 2°C warmer than that derived from the model. However, between latitudes 30°N and 36°N, the modeled SST (based on both the HR and the NCEP winds) is much warmer than that derived from the monthly MODIS satellite data.

Figs. 6(b) and 6(d) show the winter patterns for the model-derived temperature, based on the HR and NCEP winds,

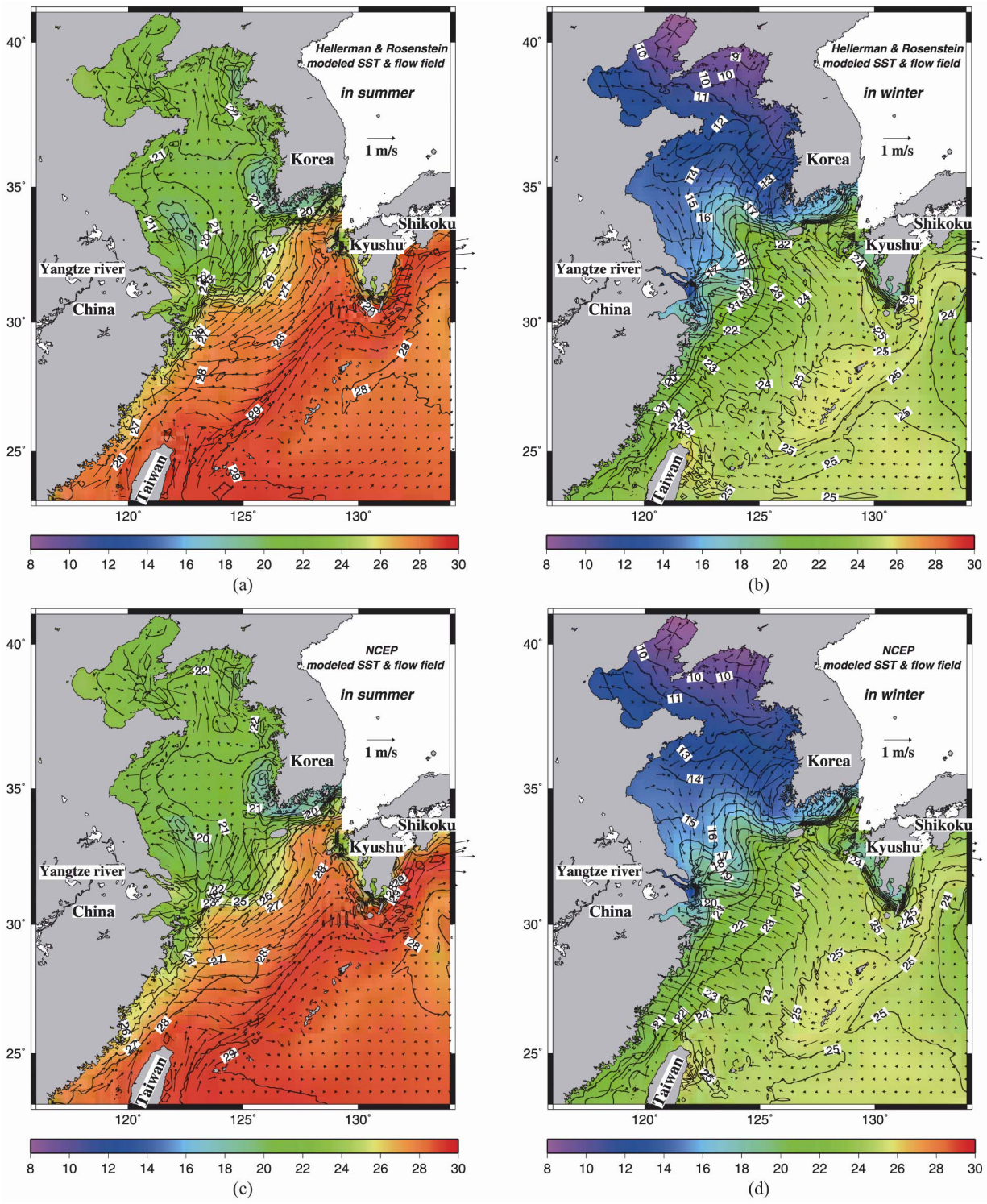

Fig. 6. Instantaneous snapshots of the model-derived surface circulation superimposed on the model-derived surface temperature for the HR wind-driven model in (a) summer and (b) winter, and for the NCEP wind-driven model in (c) summer and (d) winter.

respectively. Relative to the MODIS satellite data in winter (Fig. 7(b)), the modeled temperature results including the monthly isotherms, general patterns and the winter emergence of cold temperatures in the northern Bohai and Yellow seas are well produced by the model. For the model results the winter temperature is low in the north of the YS and BS, and higher in the southeastern regions of the ECS. The model indicates temperatures of approximately 8°C for the north of the BS (in Figs. 6(b) and 6(d)), which is similar to the MODIS satellite SST in the same region. An obvious narrow band

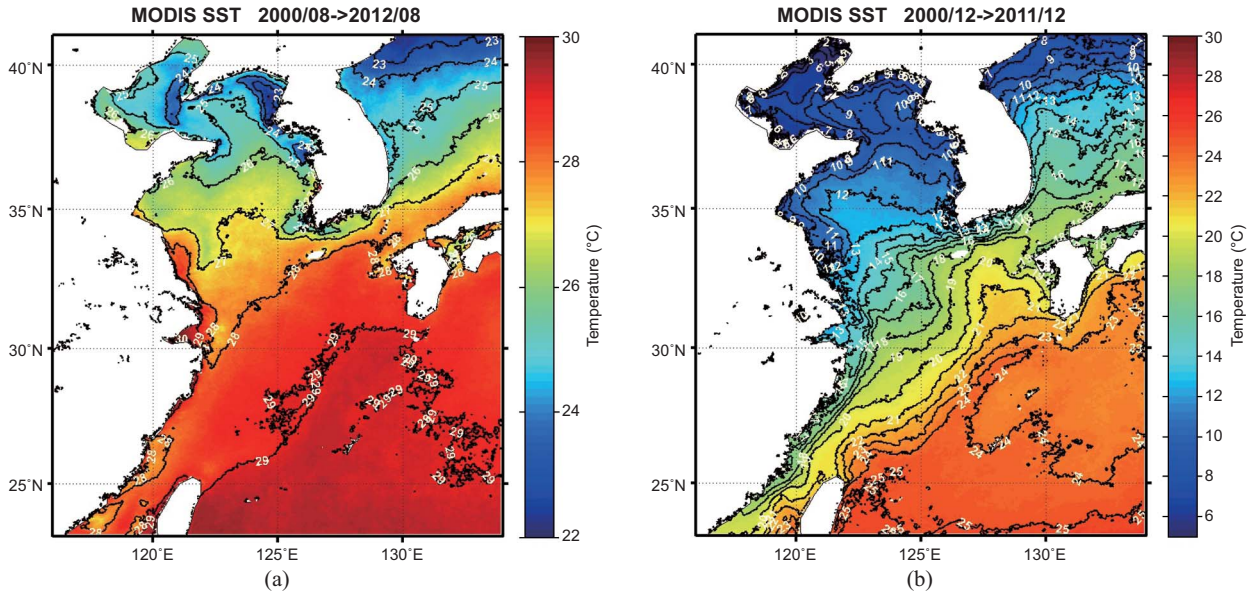

Fig. 7. Monthly climatological SST from the terra MODIS satellite. The satellite ground resolution is 4 km, and the SST data are averaged over at least 11 years (from 2000 to 2011, or from 2000 to 2012).

of low temperature isotherms (< approximately 21°C) along the southeastern China coast and extending well into the Taiwan Strait in the models (Figs. 6(b) and 6(d)) is also evident in the winter MODIS satellite SST data (Fig. 7(b)). The HR model-derived temperature seems lower than that of the NCEP model along the southeastern coast, implying that the winds in the HR model generate more cold water flowing southward than the NCEP winds.

The cold water intrusion southward of the CM can be explained by the wind stresses shown in Figs. 2(b) and 2(d). It is apparent that the HR wind stress strength in the YS (Fig. 2(b)) is stronger than that of the NCEP, but seemingly does not transport more cold water southward. The steepest north-south temperature gradient is usually centered at approximately 31°N in winter and summer. Another important feature between the CM and Tsushima Straits is a strong and sinuous isotherm (shaped like a slant-inverted Ω) that develops off the CM. Fig. 7(b) shows the typical major meander pattern in the SST derived from terra MODIS data in winter, and this is also reproduced by both the HR and NCEP wind-driven models (Figs. 6(b) and 6(d)). A possible reason for this meander off the CM is the convergence of cold waters from the YS south of Shandong peninsula with the relatively warm water from the steep north-south temperature gradient region. The meander is generally oriented in the southwest-northeast direction. The frontal mixing may be a consequence of a wind-driven current flowing southward from south of the Shandong peninsula into the warmer water regions along the China coast. Subsequently, a region of cold-warm frontal mixing develops between the CM and Tsushima Straits, leading to a southeastward excursion of the front. Although both the HR and the NCEP wind-driven models produce similar meanders to that of the terra MODIS in winter (Fig. 7(b)), the YSWC in the HR wind-driven model seems stronger than that in the NCEP wind-driven model. To this point, we can see that the isotherms along the YSWC path in the HR model protrude more north than that in the NCEP model, leading to the different meander patterns shown in Figs. 6(b) and 6(d).

VI. SURFACE SALINITY AND FRESHWATER FEATURES

Fig. 8 shows the SSS fields in summer and winter, derived from both the HR (top panels) and NCEP (bottom panels) wind-driven models. The patterns of the modeled SSS fields resemble those of the SST. Irrespective of which winds are imposed on the coupling model for summer and winter, the general distribution patterns of the models are similar, with relatively high salinity to the southeast of the study domain. For summer, the models produce similar SSS patterns for the YS and BS, with areas of low salinity around the mouth of the Changjiang River and in the western BS, respectively (Figs. 8(a) and 8(c)). Differences between Figs. 8(a) and 8(c) are evident with respect to the Changjiang River estuary and southeastern coast of China. Off the CM a low salinity water lens is detached and moved northeastward from the river mouth to the north of Jeju Island. However, a greater degree of detachment is evident in the HR model. This appears to correlate well with the northwestward wind stress, because the southeasterly winds of the HR wind field are notably much stronger than that of the NCEP wind field in summer, as shown in Figs. 2(a) and 2(c). For summer it is also evident that the distribution area of the low salinity water along

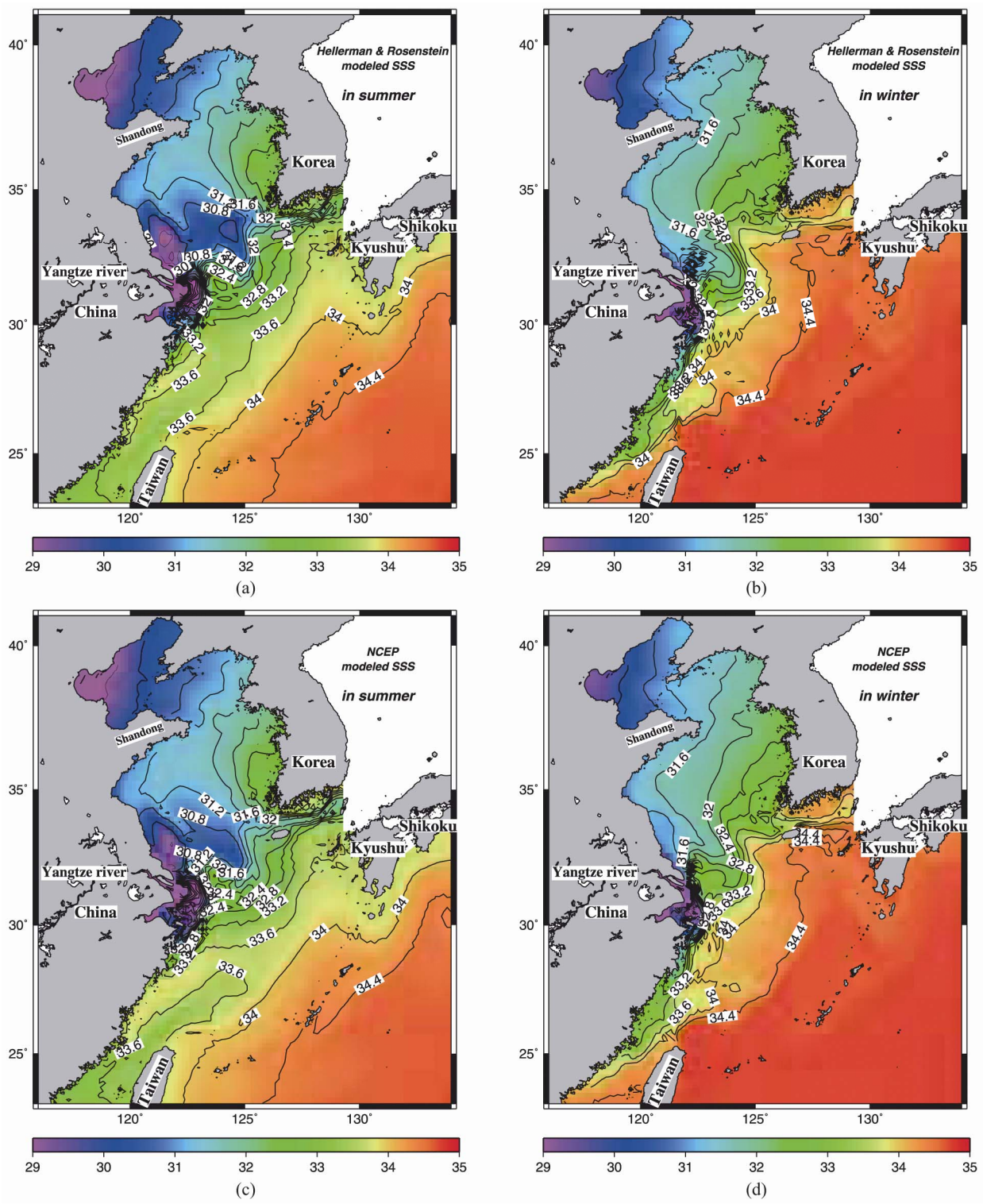

Fig. 8. Instantaneous snapshots of the model-derived surface salinity for the HR wind-driven model in (a) summer and (b) winter, and for the NCEP wind-driven model in (c) summer and (d) winter.

the southeastern China coast in the NCEP model is much larger than that in the HR model. Generally speaking, the salinity in deep layers is somewhat higher than in the surface layers. Thus, the stronger southeasterly winds suppress the occurrence of the longshore upwelling, which also can be elucidated by terms of the model temperature fields. With the prevailing northeasterly monsoon in winter, wind-driven mixing of the brackish water with the more saline water

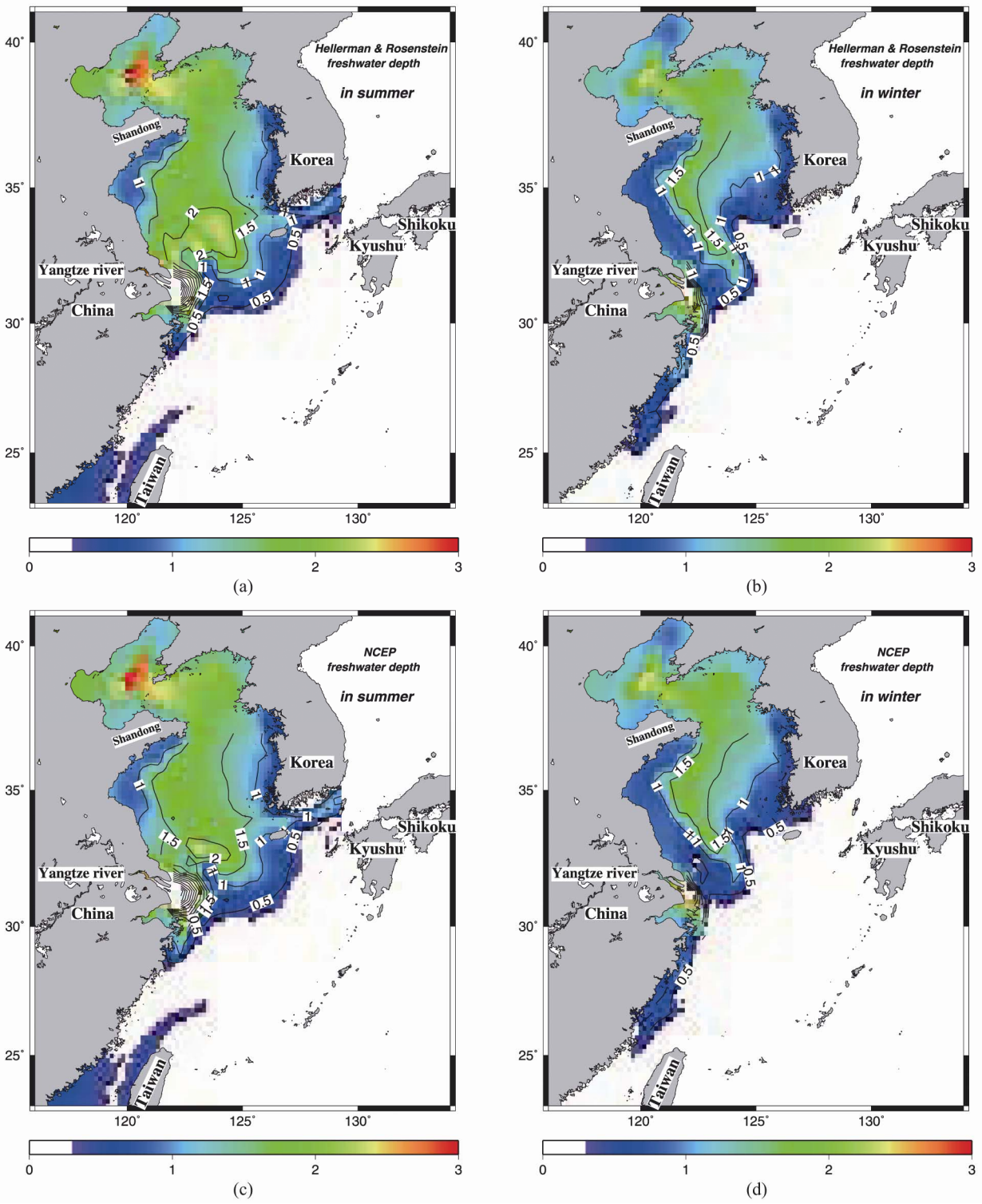

Fig. 9. Instantaneous snapshots of the model-derived equivalent depth of freshwater for the HR wind-driven model in (a) summer and (b) winter, and for the NCEP wind-driven model in (c) summer and (d) winter.

along the southeastern coast of China occurs (Figs. 8(b) and 8(d)); the remaining low-salinity plumes to the north of the CM may be residues from the previous summer. From the model results (Figs. 8(c) and 8(d)) it is sensible that exposure of the low salinity plume to the northeasterly winter monsoon forms a narrow band extending southward from the CM to the middle of the Taiwan Strait. The overall distribution patterns for the two models are similar (Figs. 8(b) and 8(d)),

although the salinity along the southeastern China coast differs slightly. As with the temperature fields, the longshore intrusion of the low salinity waters from the south of the Shandong peninsula also leads meander fronts off the CM.

In a study of the effects of reducing the Changjiang River discharge, Lee *et al*. [12] reported that in winter the ambient SSS field remains very similar to that under normal outflow conditions, even if the Changjiang River outflow is completely terminated. In other words, when the river outflow ceases the CCC still carries more and colder fresh water from the YS, flowing southward along the China coast into the Taiwan Strait. In their study, the 33.2 psu isohaline of mixed water from the YS (or from the BS) elongates to the north of the Taiwan Strait. From the SSS fields shown in Figs. 8(b) and 8(d), a large quantity of fresh water (salinity < 31.6 psu) appears in the YS and BS, steadily flows southward, and gradually mixes with the surrounding higher salinity waters to form a low-high salinity front between the CM and the Tsushima Straits; it is not easy to distinguish what is the CDW from the shelf waters. Accordingly, the distribution pattern of the CDW is expectedly examined in terms of the equivalent depth of fresh water (δ), as defined below [5].

$$\delta = \int_{-h}^{\zeta} \frac{S_a - S(z)}{S_a} dz \tag{8}$$

where S_a is the ambient salinity in the estuary, $S(z)$ is the salinity of the water column, ζ is the sea level height, and h is a reference water depth (fixed at 20.9 m if the depth of the water column is > 20.9 m). The distribution of the calculated equivalent fresh water depth (each panel in Fig. 9) shows that in winter there is a large quantity of fresh water flowing southward from the YS and the BS to the CM (and sometimes reaching into the middle of the Taiwan Strait). Irrespective of the wind stress data used in the coupling model, a layer of fresh water approximately 3 m thick emerges at the center of the BS in summer, and disappears in winter. In summer the isobaths of equivalent depth freshwater also extend along the coast from the north of the YS to the CM. A broadly equivalent freshwater pool of approximately 1.5 m thick spread from the north of the YS to the Changjiang River estuary (Figs. 9(a) and 9(b)). When the HR wind data are used in the coupling model, there is a large freshwater lens approximately 2 m thick in the northeast of the CM (Fig. 9(a)), corresponding to the distribution of the summer salinity field; this lens is reduced in the NCEP wind-driven model (Fig. 9(c)). Thus, under the same tidal forcing and hydrographic conditions, the coverage of the freshwater lens is apparently proportional to the magnitude of the northwestward wind stress. At this point, Moon *et al*. [18] had studied the process of detachment from the Changjiang plume, and noted that stronger northwestward winds tend to enhance northeast transport of the CDW across the isobaths, and wind-induced northeast transport leads to a larger offshore low salinity patch. From this, our model results for summer are consistent with this study. In addition, although a strong southeasterly wind may enhance the detachment process, summer winds such as those associated with the NCEP model (Fig. 9(c)) also resulted in detachment of the CDW, but the scale is much smaller in the same region. Theoretically, tidal forcing is also a contributor to detachment of the plume. In winter, the freshwater plume coming from the north of the YS becomes narrower than in summer (shown in Figs. 9(b) and 9(d)). Part of the fresh water from the north of the YS may readily be carried southward as a result of the strong winter monsoon, especially adjacent to the coastal boundary. The remaining fresh water hugs the China coast where it mixes with the Changjiang River water and flows southward, forming a narrow band of fresh water approximately 0.5 m thick that extends well into the north of the Taiwan Strait.

VII. DIFFERENCES IN SURFACE TEMPERATURE AND SALINITY

Fig. 10 shows the temperature and salinity anomalies derived by subtracting the results of the HR wind-driven model from those of the NCEP wind-driven model. Fig. 10(a) shows that the temperature anomaly in summer is distributed between the CM and the southern tip of the Korean peninsula, extending into the southeastern China coast. The temperature anomaly is approximately +0.5°C north of latitude 30°N, and approximately −1.0°C in the region along the southeastern China coast. The temperature to the north of the CM determines in the HR wind-driven model is higher than that in the NCEP model, and is lower along the southeastern China coastline. In winter, the major anomalies are between the CM and the Korean peninsula, and are positive to the northeast of the CM and western Korean peninsula (Fig. 10(b)). Another feature is also noteworthy is that the YSWC protrudes northward from its path under the stronger wind stresses in the HR model. Beyond the YSWC, the distribution of temperature anomalies varys among seasons. An outstanding feature, like the summer plume, is the emergence to the northeast of the CM under the prevailing strong northwesterly monsoon in winter, as shown in Fig. 10(b). The greatest anomaly which commonly reaches 1.5°C and in some cases exceeds 2°C is evident near the CM. With respect to the salinity anomalies in summer, a small patch of +0.5 psu is evident between the CM and the Korean peninsula, and a small patch of −2 psu is distributed to the south of the CM (Fig. 10(c)). For winter, the salinity anomalies (Fig. 10(d)) are positive throughout the study area, but are particularly concentrated along the southeastern China coast, and slightly positive salinity anomalies are distributed between the CM and the southeastern Korean peninsula.

For both temperature and salinity anomalies, the greatest differences are always in the vicinity of the CM, or between the CM and the Korean peninsula. Thus, the different wind data used in the tide-circulated coupling models have a major influence in the area between the CM and the Korean

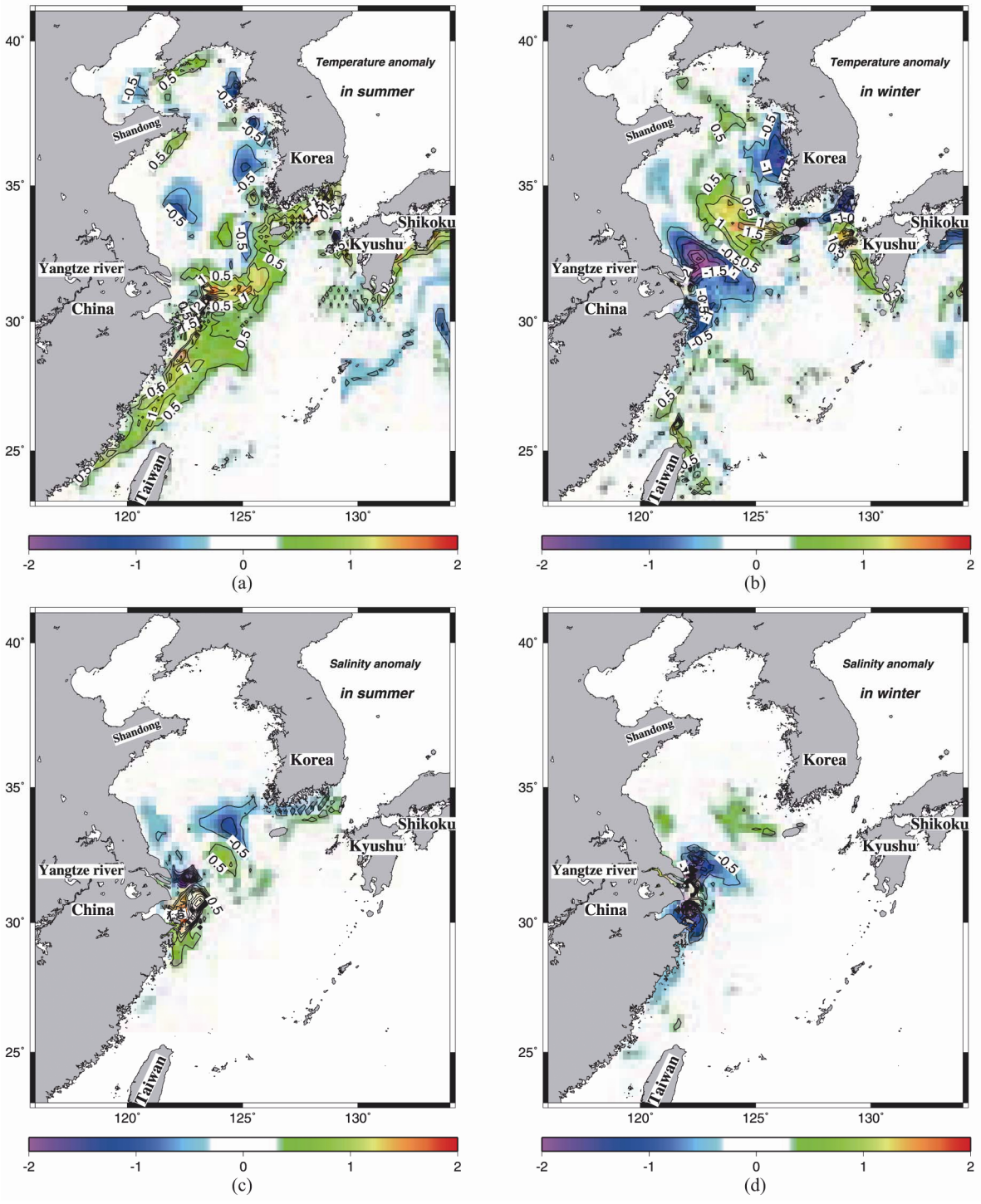

Fig. 10. Anomalies derived by subtracting the results of HR wind-driven model from those of the NCEP model. Top panels: temperature anomalies in (a) summer and (b) winter. Bottom panels: salinity anomalies in (c) summer and (d) winter.

peninsula, and involve anomalies of 1.5°C for temperature and > 2 psu for salinity (Fig. 10).

VIII. DISCUSSION AND CONCLUSIONS

In the study, we apply different wind magnitudes in a 3-D tide-circulated coupling model to assess differences in the wind effects on the SST, SSS and the equivalent freshwater of depth in the ECS region. In other words, two wind stress datasets (the HR and NCEP wind datasets) are applied to a 3-D tide-circulated coupling model for the ECS region. Based on common monthly temperature and salinity fields, we compare

the effects of the wind datasets on the parameters SST, SSS and the equivalent depth of freshwater. The dynamic behavior of the different wind strength fields produces significant effects on these hydrographic data.

A strong and sinuous frontal feature involving isotherms with the appearance of a slant-inverted Ω is developed off the CM in winter (see Fig. 7(b)). The feature derived from the modeled results shows SST and a major meander pattern typical of the monthly climatological SST of terra MODIS satellite data for winter. In interpreting the phenomenon of the meander, its pattern probably results from convergence of cold water from the YS off the Shandong peninsula with relatively warm water from the region of the steep north-south temperature gradient, producing a meandering front oriented in a southwest-northeast direction off the CM. The HR model results indicate that the YSWC increases in strength because of greater northwesterly wind stress; weakening of the wind stress such as the NCEP winds could reduce the strength of the YSWC, causing it to retreat. Relative to the NCEP, the HR wind-driven model produces a large freshwater lens (approximately 2 m in depth) to the northeast of the CM during summer. From this point, the prevailing southwesterly monsoon seems to be the most important factor associated with the area of the Changjiang River plume in summer, but neither wind model distinguishes it from the contributors in winter. Moon *et al*. [18] noted that stronger northwestward winds tend to enhance northeastward detachment of the CDW across the isobaths, which to this point is a finding consistent with our model results.

In addition, there is at least a 1.5°C variation in temperature and a 2 psu variation in salinity in the region between the CM and the Korean peninsula using the two different wind datasets. The model results show that the major differences in the SST and SSS fields usually occurs between latitudes 30°N and 35°N, which is also the region having the steepest north-south temperature gradient. It is obvious that the stronger southeasterly winds clearly suppress the occurrence of the longshore upwelling, evidently elucidated in the model temperature fields.

ACKNOWLEDGMENTS

Author H.J.L. was sponsored by the National Science Council (Taiwan) through grants NSC-100-2611-M-019-003.

REFERENCES

1. Beardsley, R. C., Limeburner, R., Yu, H., and Cannon, G. A., "Discharge of the Changjiang (Yangtze River) into the East China Sea," *Continental Shelf Research*, Vol. 4, pp. 57-76 (1985).
2. Chao, S. Y., "River-forced estuarine plume," *Journal of Physical Oceanography*, Vol. 18, pp. 72-88 (1988).
3. Chao, S. Y., "Circulation of the East China Sea, a numerical study," *Journal of the Oceanographical Society of Japan*, Vol. 46, pp. 273-295 (1991).
4. Chen, X., Wang, X., and Guo, J., "Seasonal variability of the sea surface salinity in the East China Sea during 1990-2002," *Journal of Geophysical Research*, Vol. 111, C05008, DOI: 10.1029/2005JC003078 (2006).
5. Choi, B. J. and Wilkin, J. L., "The effect of wind on the dispesal of the Hudson river plume," *Journal of Physical Oceanography*, Vol. 37, pp. 1878-1897 (2007).
6. Dean, R. G. and Dalrymple, R. A., *Water Wave Mechanics for Engineers and Scientists*, Prentice-Hall, Inc., Englewood Cliffs, N. J. (1984).
7. Foreman, M. G. G. and Henry, R. F., *Tidal Analysis Based on High and Low Water Observations*, Pacific Marine Science Report, 79-15, Institute of Ocean Sciences, Patricia Bay, Sidney, British Columbia (1979).
8. Guo, X. and Yanagi, T., "Three-dimensional structure of tidal current in the East China Sea and the Yellow Sea," *Journal of Oceanography*, Vol. 54, pp. 651-668 (1998).
9. Hellerman, S. and Rosenstein, M., "Normal monthly wind stress over the world ocean with error estimates," *Journal of Physical Oceanography*, Vol. 13, pp. 1093-1104 (1983).
10. Hu, C. K., Chiu, C. T., Chen, S. H., Jan, S., and Tseng, Y. H., "Numerical simulation of barotropic tides around Taiwan," *Terrestrial, Atmospheric and Oceanic Sciences*, Vol. 21, No. 1, pp. 71-84 (2010).
11. Lee, H. J. and Chao, S. Y., "A climatological description of circulation in and around the East China Sea," *Deep-Sea Research II*, Vol. 50, pp. 1065-1084 (2003).
12. Lee, H. J., Chao, S. Y., and Liu, K. K., "Effects of Reduced Yangtze River Discharge on the Circulation of Surrounding Seas," *Terrestrial, Atmospheric and Oceanic Sciences*, Vol. 15, No. 2, pp. 1-23 (2004).
13. Lee, H. J. and Liu, K. K., "Tidal effects on Changjiang plume dispersal in the East China Sea," *Journal of Marine Science and Technology*, Vol. 21, No. 3, pp. 342-352 (2013).
14. Lefevre, F., Provost, C. L., and Lyard, F. H., "How can improve a global ocean tide model at a regional scale: A test on the Yellow Sea and the East China Sea," *Journal of Geophysical Research*, Vol. 105, No. C4, pp. 9707-8725 (2000).
15. Lie, H. J. and Cho, C. H., "On the origin of the Tsushima Warm Current," *Journal of Geophysical Research*, Vol. 99, No. C12, pp. 25081-25091 (1994).
16. Lie, H. J., Cho, C. H., Lee, J. H., and Lee, S., "Structure and eastward extension of the Changjiang River plume in the East China Sea," *Journal of Geophysical Research*, Vol. 108, No. C3, pp. 1-14, DOI: 10.1029/2001JC001194 (2003).
17. Liu, K. K., Gong, G. C., Shyu, C. Z., Pai, S. C., Wei, C. L., and Chao, S. Y., "Response of Kuroshio upwelling to the onset of the northeast monsoon in the sea north of Taiwan: Observations and a numerical simulation," *Journal of Geophysical Research*, Vol. 97, pp. 12511-12526 (1992).
18. Moon, J. H., Hirose, N., Yoon, J. H., and Pang, I. C., "Offshore detachment process of the low-salinity water around Changjiang bank in the East China Sea," *Journal of Physical Oceanography*, Vol. 40, pp. 1035-1053 (2010).
19. Nitani, H., "Beginning of the Kuroshio," in: Stommel, H. and Yoshida, K. (Eds.), *Kuroshio*: *Physical Aspects of the Japan Current*, University of Washington Press, pp. 129-163 (1972).
20. Pugh, D. T., *Tides, Surges and Mean Sea-Level*, John Wiley and Sons, New York (1987).
21. Sarmiento, J. L. and Bryan, K., "An ocean transport model for the North Atlantic," *Journal of Geophysical Research*, Vol. 87, pp. 394-408 (1982).
22. Wu, H., Zhu, J., Shen, J., and Wang, H., "Tidal modulation on the Changjiang River plume in summer," *Journal of Geophysical Research*, Vol. 116, C08017, DOI: 10.1029/2011JC007209 (2011).
23. Yanagi, T., Morimoto, A., and Ichikawa, K., "Co-tidal and co-range charts for the East China Sea and the Yellow Sea derived from satellite altimetric data," *Journal of Oceanography*, Vol. 53, pp. 303-309 (1997).